Naval Research Laboratory

Washington, DC 20375-5320

NRL/MR/8221--18-9811

Towards a Hybrid Mechanically-Pumped Loop Heat Pipe: Investigation of Bearingless Micro-Pumps

Gabriel B. Goodwin
Jesse R. Maxwell
Evan W. Hyde

Naval Center for Space Technology
Naval Research Laboratory

September 4, 2018

REPORT DOCUMENTATION PAGE

Form Approved
OMB No. 0704-0188

1. REPORT DATE *(DD-MM-YYYY)*	**2. REPORT TYPE**	**3. DATES COVERED** *(From - To)*
04-09-2018	Memorandum Report	July 2016 - July 2018

4. TITLE AND SUBTITLE

Towards a Hybrid Mechanically-Pumped Loop Heat Pipe: Investigation of Bearingless Micro-Pumps

5a. CONTRACT NUMBER

5b. GRANT NUMBER

5c. PROGRAM ELEMENT NUMBER

6. AUTHOR(S)

Gabriel B. Goodwin, Jesse R. Maxwell and Evan W. Hyde

5d. PROJECT NUMBER

5e. TASK NUMBER

5f. WORK UNIT NUMBER
82-1J09-08

7. PERFORMING ORGANIZATION NAME(S) AND ADDRESS(ES)

Naval Research Laboratory
4555 Overlook Avenue, SW
Washington, DC 20375-5320

8. PERFORMING ORGANIZATION REPORT NUMBER

NRL/MR/8221--18-9811

9. SPONSORING / MONITORING AGENCY NAME(S) AND ADDRESS(ES)

10. SPONSOR / MONITOR'S ACRONYM(S)
NRL

11. SPONSOR / MONITOR'S REPORT NUMBER(S)

12. DISTRIBUTION / AVAILABILITY STATEMENT

DISTRIBUTION STATEMENT A: Approved for public release; distribution is unlimited.

13. SUPPLEMENTARY NOTES

14. ABSTRACT

As the electronics systems aboard air and spacecraft grow in scale and complexity, so too does the heat generated by those systems. A high-heat flux, compact, maintenance-free cooling system is required to meet the increased demand for heat removal. Loop heat pipes are robust and effective thermal management systems that are long-life and maintenance-free, making them ideal for use in unmanned spacecraft. Integrating a mechanical pump into a loop heat pipe system can drastically improve the system's heat removal capacity through increased mass flowrate. Like loop heat pipes, magnetically-driven bearingless pumps are also maintenance-free, which is a necessity in the space environment. This work details the modeling of a low-flowrate, magnetically-driven bearingless centrifugal pump and a computational fluid dynamics study of the pump's operation and performance under a range of conditions that are typical to the demands of a satellite thermal management system. The purpose of this computational study is to investigate the failure mechanism of a bench-test unit that was unable to generate a pressure head with its intended working fluid of ammonia. Model development, validation, and pump performance with multiple working fluids are discussed. The cause of the pump's failure is investigated. Following the failure mode investigation, an alternative pump design was identified and several units acquired and tested with a variety of working fluids, including ammonia. These results and plans for integration in a hybrid loop heat pipe are discussed.

15. SUBJECT TERMS

16. SECURITY CLASSIFICATION OF:			**17. LIMITATION OF ABSTRACT**	**18. NUMBER OF PAGES**	**19a. NAME OF RESPONSIBLE PERSON**
a. REPORT	**b. ABSTRACT**	**c. THIS PAGE**			Gabriel B. Goodwin
Unclassified Limited	Unclassified Limited	Unclassified Limited	Unclassified Limited	27	**19b. TELEPHONE NUMBER** *(include area code)* (202) 404-2710

Standard Form 298 (Rev. 8-98)
Prescribed by ANSI Std. Z39.18

This page intentionally left blank.

Contents

Nomenclature

$\frac{dU}{dy}$	Mean velocity gradient
$\dot{m}$	Mass flowrate [g/s]
p_i	Static pressure [psi]
p_i	Static pressure at inlet [psi]
p_o	Static pressure at outlet [psi]
Q	Volumetric flowrate [m^3/s]
r_i	Radial distance from impeller core to inlet surface [m]
r_o	Radial distance from impeller core to vane tip [m]
$\vec{r}$	Position vector in rotating frame [m]
T	Torque [oz-in]
$\vec{u}$	Absolute velocity [m/s]
$\vec{u_r}$	Relative velocity [m/s]
$\overline{uv}$	Reynolds stress
Δp	Differential pressure [psid]
λ	Latent heat of vaporization [J/kg]
μ	Viscosity [Pa-s]
ν_e	Eddy viscosity [Pa-s]
ρ	Liquid density [kg/m^3]
σ	Surface tension [N/m]
$\vec{\Omega}$	angular velocity in rotating frame [rpm]
ω	angular velocity [rpm]

1 Introduction

Advances in electronics miniaturization have resulted in an increase in the density of electronics on board satellites and other spacecraft. The increased heating generated by these systems must be met with improved thermal management to ensure the operating temperatures of the various subsystems on board are kept within design limits. Magnetically-driven bearingless pump technology has the potential to supplement the reliable, but limited, loop heat pipe system to provide advanced thermal management in unmanned spacecraft. Current limits on loop heat pipe transport capability are primarily viscous losses and the low pressure head generated by capillary pumping. Integration of a mechanical pump in a hybrid loop heat pipe system to increase flowrate of the refrigerant allows for improved heat transport capacity and electronics density.

The advantage to a magnetically-driven bearingless pump over traditional positive displacement or centrifugal pumps is that there is no driving shaft between the motor and the impeller, so no bearing assembly is required. As such, no residue is produced through mechanical wear that will clog a loop heat pipe's sub-micron pores. This concept, first developed for pumping blood [1–3], has great potential in pumping refrigerants in maintenance-free and long-life thermal systems. The pump is hermetically sealed against its surroundings, preventing contaminants from entering the loop. A schematic of such a pump is shown in Fig. 1. This unit was intended for use with liquid anhydrous ammonia (NH_3) as the working fluid, as it is commonly used in loop heat pipes due to its high latent heat of vaporization, λ, and liquid transport factor, LTF. The liquid transport factor is a metric for ranking two-phase heat pipe fluids,

$$LTF = \frac{\rho\sigma\lambda}{\mu} \tag{1}$$

where ρ is liquid density, σ is surface tension, and μ is liquid viscosity. A solid model of the pump and rotor assembly is shown in Fig. 2. Permanent magnets embedded inside the rotor cause it to spin when the motor imposes a magnetic field. The induced centrifugal gravity field within the casing causes the rotor, which has approximately 70% the density of the fluid, to float to the center of the casing. The rotor stays centered within the casing, maintaining a small clearance that is filled with the working fluid, negating the need for a bearing or lubricant. A controller regulates the magnetic field imposed by the motor to maintain the rotor speed at any desired level. Both the pump and casing are aluminum. The pump dimensions are listed

Manuscript approved September 4, 2018.

in Table 1. The impeller has four vanes, with a radius of curvature of 3 mm at the point of maximum curvature along the vane wall.

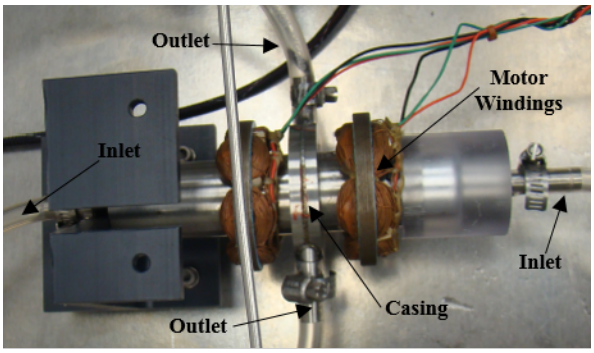

Fig. 1. Bearingless ammonia pump installed in a closed loop for initial concept validation.

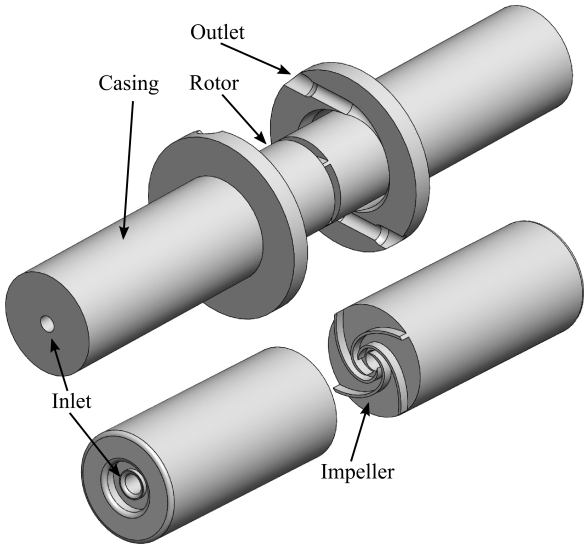

Fig. 2. Solid model of the bearingless pump. (Above) Casing and rotor assembly (Below) Rotor with integrated impeller.

A series of experimental tests was conducted at the US Naval Research Laboratory in 2009 to validate the design of the pump shown in Fig. 1, both with a Freon equivalent fluid and with ammonia. Ammonia is the more desirable fluid, due to its higher LTF. At 22°C and 185 psia, liquid ammonia has an LTF of 1.37×10^{11} W/m^2. At these same conditions, Freon (R-11) has an LTF of 1.25×10^{10} W/m^2. The pump operated successfully with the Freon equivalent, producing a differential pressure of 6.25 psi at 5,600 rpm. When run with ammonia, the pump stalled at 800 rpm prior to generating any pressure head. Temperatures at the inlets and outlets of the pump housing indicated that, with ammonia, fluid would flow in one inlet and out of the other, such that the pump was "short-circuited" and a miniature loop was formed within the pump housing. Following the pump failure with ammonia, a third-party was contracted

Table 1. Bearingless pump dimensions, units of mm.

rotor length	112.25
rotor diameter	25.5
casing length (both halves)	145.7
casing outer diameter at ends	29.2
casing outer diameter at center	50.9
casing inner diameter	28.3
inlet, outlet, rotor core diameter	4.7

to perform a computational fluid dynamics (CFD) simulation of the pump's operation at its design point with ammonia of 12,000 rpm. Based on those simulation results, the pump was predicted to produce a differential pressure of 12 psi at 12,000 rpm. No other speeds or operating conditions were simulated at that time.

This paper discusses the development of a computational model to simulate the flow through the NRL bearingless pump across a range of operating conditions and speeds in order to investigate the cause of failure. The determination of boundary and initial conditions, meshing parameters, assignment of reference frames, model validation, and predicted pump performance are examined. Possible causes of the pump's failure with ammonia are discussed. An alternative to the NRL bearingless pump, a commercially available magnetically coupled bearingless pump, was tested with a variety of working fluids in several configurations in the NRL Advanced Two Phase Facility. This paper presents those results and plans for integration into a mechanically pumped hybrid loop heat pipe system.

2 NRL Bearingless Pump Model Development

2.1 Simplified Geometry & Initial Condition Determination

Prior to computing the flow through the full pump model, flow through a single vane domain and as well as through the impeller section was simulated in order to determine the initial conditions for the full model simulation as well as to get a basic understanding of flow quality in the impeller section. The solid model of the pump casing and rotor/impeller assembly, modeled using Solidworks CAD software, is shown in Fig. 2. The single vane domain and impeller models are shown in Fig. 3. All CFD was performed using ANSYS Fluent V16.2.

To determine the initial conditions for the single vane domain, the pressure differential in the radial direction resulting from the centrifugal force of the pump's rotation [4] was calculated

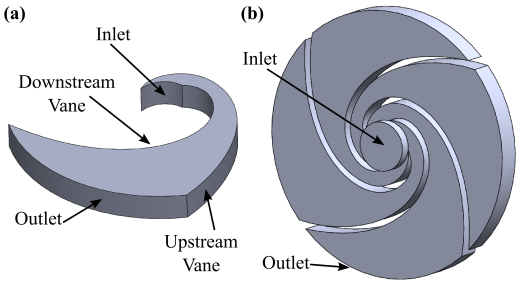

Fig. 3. (a) Model of the single vane domain. (b) Model of the impeller section.

by

$$\Delta p = p_o - p_i = \frac{1}{2}\rho\omega^2(r_o^2 - r_i^2) \tag{2}$$

where Δp is the pressure differential, p_o is the static pressure at the outlet, p_i is the static pressure at the inlet, ρ is the fluid density, ω is the impeller's angular velocity, r_o is the radial distance from the impeller core to vane tip, and r_i is the radial distance from the impeller core to the inlet surface. The resulting pressure differential was used as the initial condition in Fluent to determine the mass flowrate, $\dot{m}$, through the domain for a given pressure condition and angular velocity. With each of these parameters known, the problem was fully constrained. A gauge pressure of zero was used as the inlet condition and a gauge pressure of Δp was used as the outlet condition. The fluid reference frame was initialized to rotate at the angular velocity corresponding to the specified mass flowrate. Mass flowrate through the domain was tracked until the solution converged on a steady-state value. These values for the operating range of the bearingless pump are shown in Table 2. For these intial simulations, a laminar model was used. For subsequent simulations, using both the impeller and full model geometries, the mass flowrate was used as an inlet boundary condition and an outflow boundary condition was applied to the outlet to enforce mass conservation through the domain.

When initialized using a rotating reference frame, the single vane domain simulations showed the expected static pressure profile, as shown in Fig. 4(a). Recirculation was evident based on relatively strong eddy viscosity, ν_e, near the outlets, as shown in the impeller domain in Fig. 4(b). Eddy viscosity is a useful parameter for characterizing the turbulent stress in the flow [5, 6]. It is expressed as

Table 2. Calculated Δp and mass flowrate for pump speeds in the operating range of 800 to 12000 rpm.

ω (rpm)	Δp (psi)	$\dot{m}$ (g/s)
800	0.049	0.317
1,800	0.246	0.981
2,800	0.596	1.603
3,800	1.098	2.218
4,800	1.752	2.936
6,000	2.738	3.691
8,000	4.868	4.879
10,000	7.606	6.158
12,000	10.953	7.347

$$-\overline{uv} = \nu_e \frac{dU}{dy} \tag{3}$$

where $\overline{uv}$ is the Reynolds stress, and dU/dy is the mean velocity gradient. These simulations were run using a $\kappa - \omega$ SST viscous model. All surfaces were modeled as no-slip walls with parameters for smooth aluminum (roughness height of 1×10^{-3} mm and roughness constant of 0.5). The single vane domain consisted of 1.2×10^5 computational elements and the impeller domain consisted of 1.9×10^6.

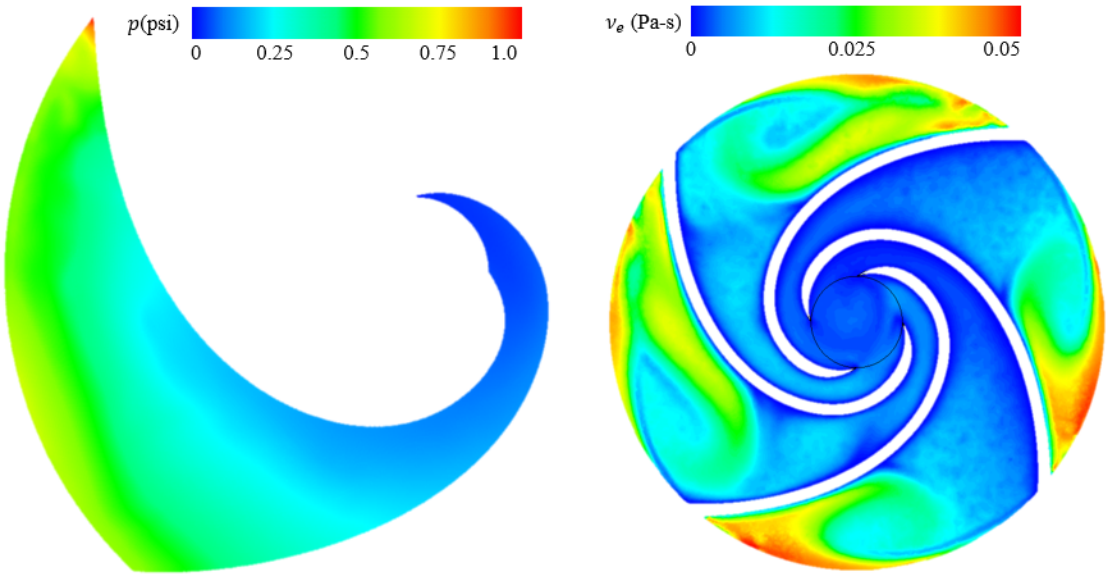

Fig. 4. (a) Static pressure contour of single vane domain and (b) Eddy viscosity contour of impeller domain for ω = 2,800 rpm and $\dot{m}$ = 1.603 g/s

2.2 Full Model Development & Validation

In order to understand the dynamics of the entire bearingless pump system, not just the fluid interaction with the impeller section, a full system model was developed. A tetrahedral mesh was used with 4.9 $\times 10^6$ elements, a minimum face size of 9.6 $\times 10^{-2}$ mm, and a maximum face size of 0.8 mm. Additional refinement was used at the impeller section, inlets, and near all rotating surfaces. The full model is shown in Fig. 5. Two different fluid zones were used: a zone with a rotating reference frame to model the rotational flow of the impeller (marked 'R' in Fig. 5(b)) and a zone with a stationary reference frame to model flow through the rest of the domain (marked 'S' in Fig. 5(b)). Rotational speed in the rotating reference frame was set at an angular velocity equal to the pump's operating speed. A $\kappa - \omega$ SST viscous model was used. The mass flowrate correpsonding to the specified angular velocity (from Table 2) was used as an inflow boundary condition to both inlets, with $\dot{m}/2$ flowing into each inlet. An outflow boundary condition was assigned to both outlets, with an equal flowrate through each. As in the simplified geometries, all surfaces were modeled as no-slip walls with parameters for smooth aluminum (roughness height of 1×10^{-3} mm and roughness constant of 0.5). The walls of the casing were stationary and the walls of the rotor were assigned a rotational speed equal to the angular velocity of the impeller. A semi-implicit method for pressure linked equations (SIMPLE) pressure-based solver was used with an absolute velocity formulation to implicitly solve the incompressible Navier-Stokes equations and converge on a steady-state solution. Second order, upwind schemes were used for spatial discretization. Convergence was determined based on residuals, and other parameters of interest, falling to steady-state, asymptotic values. Outlet pressure was a primary factor in determination of convergence; this is discussed in detail in Sec. 33.3. Constant fluid properties were used.

To validate the model, a test case was run for comparison against available experimental data. During the bench-unit testing at NRL in 2009, the pump failed to produce a pressure head with ammonia as the working fluid, but produced a pressure head of 6.25 psi with a Freon equivalent at a speed of 5,600 rpm. A simulation was performed, using the full model, at 5,600 rpm using Freon-12 as the working fluid. At this speed, a mass flowrate of 8.347 g/s was used as the inflow condition, which was calculated by the method previously described. The model produced a pressure head of 6.26 psid, which is calculated by subtracting the area-weighted average of pressure at the inlet faces from the outlet faces. The model also showed agreement with the results from the previous CFD simulation, discussed in Sec. 1, in which the pump

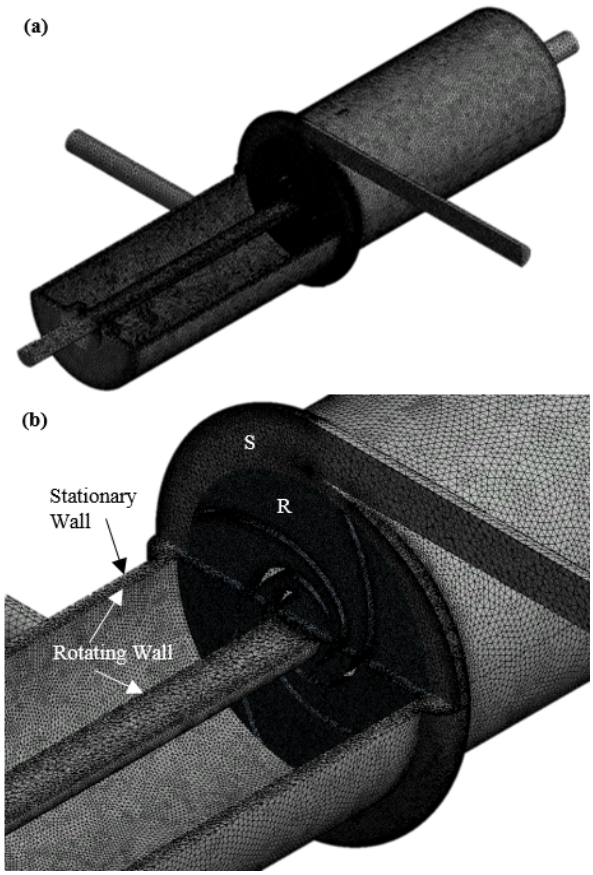

Fig. 5. (a) Meshed full model with quarter-section cutaway. (b) Impeller section. Stationary fluid zone 'S' and rotating fluid zone 'R' shown.

produced 12 psid at 12,000 rpm with ammonia. The model described in this paper produced 14.18 psid at 12,000 rpm with ammonia.

A grid independence study was performed, with results shown in Fig. 6. Identical models, with grid element counts ranging from 3×10^6 to 18.7×10^6, were run under identical settings and initial conditions. Relative error was determined by comparison of the area-averaged outlet pressure with the value obtained using the highest grid resolution (24.7×10^6 elements) in order to characterize the error convergence and global method order. The solution method was shown to be globally first order, as expected due to local second order spatial accuracy. This is indicated by the slope of -0.9025 for the trendline shown in Fig. 6, which plots log(Number of Elements) vs. log(Relative Error). The grid resolution used to perform the simulations described in this paper achieves 7.7% accuracy relative to the finest grid tested; it was selected due to its decreased computational expense while still resolving the parameters of interest and flow structures well enough to characterize pump performance and flow quality.

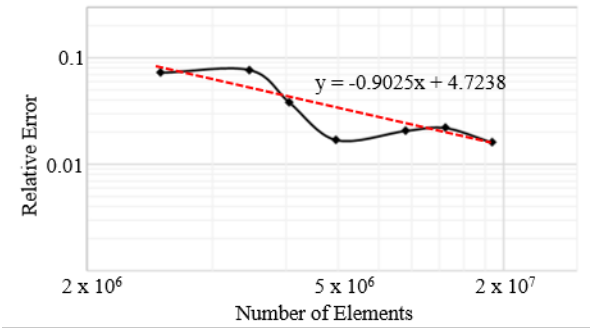

Fig. 6. Grid convergence study with trendline shown for log(Number of Elements) vs. log(Relative Error).

3 Computational Modeling of NRL Bearingless Pump

3.1 Predicted Performance

In order to identify the pump's failure mechanism with ammonia, a series of simulations was performed to characterize the flow quality through the pump and its ability to produce a pressure head from low speeds (800 rpm) up to the design point (12,000 rpm). Torque required to spin the rotor at the designated speed, differential pressure, and efficiency are plotted as a function of pump speed, ω (in rpm), in Fig. 7. Efficiency is defined as $Q\Delta p/\omega T$, where Q is volumetric flowrate and T is torque. Predicted Δp and required torque increase at a rate of ω^2. Efficiency increases with increasing ω until reaching an asymptotic value of approximately 3.5%. The data point for the pump's operation with Freon (from both experimental and simulation results) is overlaid for comparison. To produce the same Δp with ammonia, the rotor must spin at a factor of 1.5 times the speed required with Freon. Similarly, the torque required to spin the rotor at 5,600 rpm is 1.5 times greater with Freon than it is with ammonia. The mass flowrate as a function of Δp trend closely follows the theoretical curve until a Δp of approximately 3 psid, at which point the simulation begins to produce a higher Δp than theory predicts. One must note that the comparison of theory and calculated result is not a direct comparison of values at the same pump location. The theoretical value predicts the pressure differential from the impeller core to the outer edge of the vane domain, using Eq. 2, and the calculated value is the pressure differential from the inlets to the outlets of the full model, as shown in Fig. 2. The slowing of the fluid after exit from the impeller through contact with the walls at the outlets causes an additional increase in Δp as the kinetic energy is converted to static pressure, resulting in a Δp that is slightly higher than the theoretical value.

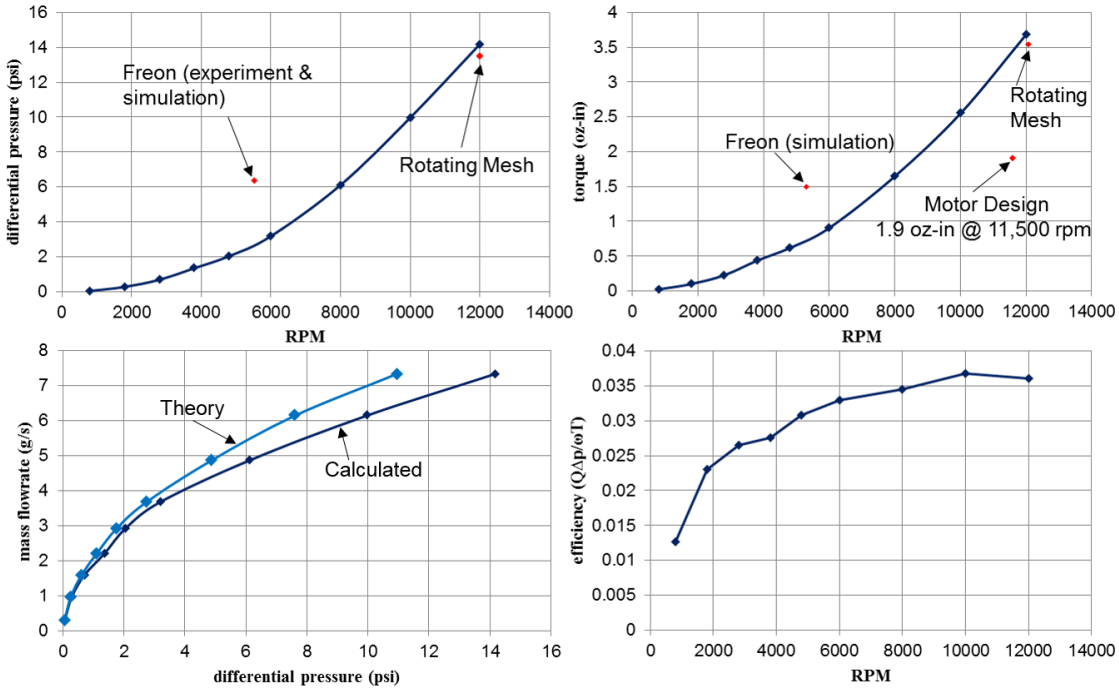

Fig. 7. Pump performance curves with ammonia. Results with Freon shown for comparison.

3.2 Rotating Fluid Zone Model

An additional simulation of pump operation at 12,000 rpm was performed using a rotating mesh in the impeller fluid zone, instead of a rotating reference frame. In the case of a rotating reference frame, terms for the angular velocity are added to the fluid equations and the equations are solved on a stationary grid. Equation 4 is the left-hand side of the conservation of momentum equation in the inertial reference frame, Eqn. 5 relates the absolute velocity, $\vec{u}$, and relative velocity, $\vec{u_r}$, and Eqn. 6 is the left-hand side of the momentum equation in a rotating reference frame, written in terms of absolute and relative velocities:

$$\frac{\partial}{\partial t}(\rho\vec{u}) + \nabla \cdot (\rho\vec{u}\vec{u}) \tag{4}$$

$$\vec{u_r} = \vec{u} - (\vec{\Omega} \times \vec{r}) \tag{5}$$

$$\frac{\partial}{\partial t}(\rho\vec{u}) + \nabla \cdot (\rho\vec{u_r}\vec{u}) + \rho(\vec{\Omega} \times \vec{u}) \tag{6}$$

where $\vec{r}$ is the position vector in the rotating frame and $\vec{\Omega}$ is the angular velocity vector in the rotating frame. In terms of relative velocities in the rotating reference frame, the left-hand side

is given by Eqn. 7:

$$\frac{\partial}{\partial t}(\rho\vec{u_r}) + \nabla \cdot (\rho\vec{u_r}\vec{u_r}) + \rho(2\vec{\Omega} \times \vec{u_r} + \vec{\Omega} \times \vec{\Omega} \times \vec{r}) + \rho\frac{\partial\vec{\Omega}}{\partial t} \times \vec{r} \tag{7}$$

where $\rho(2\vec{\Omega} \times \vec{u_r} + \vec{\Omega} \times \vec{\Omega} \times \vec{r})$ is the Coriolis force.

Rotating the mesh is the most accurate way to model the rotation of the impeller, as in this case the fluid rotation is caused by the body force of the vanes and impeller walls acting on the fluid. When using a rotating mesh, the mesh position is recalculated at every time step and the fluid equations are solved implicitly until the solution converges for that time step, then the time step advances. In this way, a transient solution can be simulated prior to convergence upon a steady-state solution, where the flow field remains relatively unchanged between time steps. Rotating the mesh required at least four times the number of CPU hours in the case of ω = 12,000 rpm than simply using a rotating reference frame. As shown in the plots for differential pressure and torque as a function of pump speed in Fig. 7, the Δp and T differed by 1.8% and 0.79%, respectively, between these two methods. Due to this quantitative agreement between methods, and the increased computational expense of using a rotating mesh, a rotating reference frame was used in all other calculations.

3.3 Convergence

Because of the transient flow conditions in this system, such as the recirculation in the impeller, it does not converge upon a true steady-state solution. Since pump performance is typically characterized by the pressure head generated, the area-averaged pressure at the pump outlets was selected as a monitor for convergence, in addition to the residual errors in the iterative solutions to the fluid equations. Figure 8 shows the area-averaged outlet pressure as a function of iteration for the cases of ω = 12,000 rpm with a rotating reference frame at the impeller and with a rotating mesh. With the rotating mesh, the solution begins to oscillate about an asymptotic mean value of 14.37 psi at approximately 15,000 iterations. Convergence upon an asymptotic mean value of 14.34 psi occurs more quickly when using a rotating reference frame, after approximately 2,000 iterations.

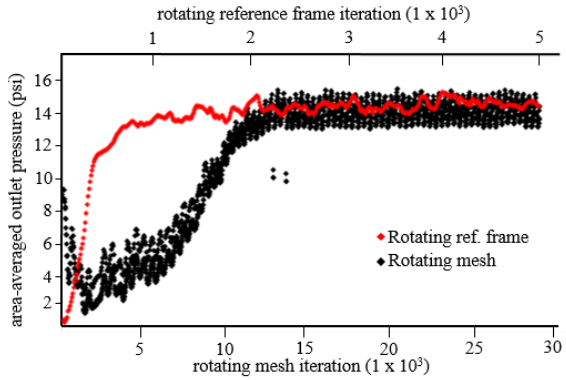

Fig. 8. Area-averaged outlet pressure as a function of number of iterations for ω = 12,000 rpm with both a rotating mesh and a rotating reference frame.

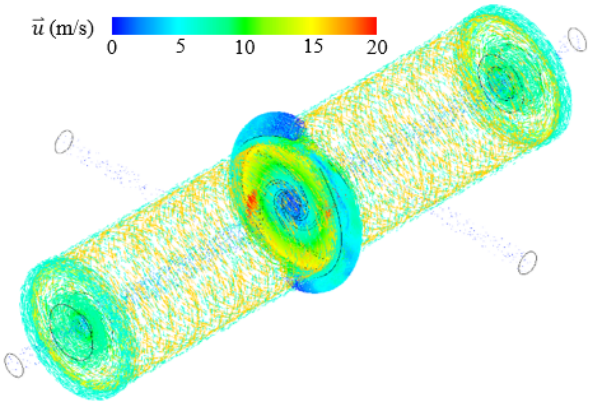

Fig. 9. Vector field of absolute velocity, $\vec{u}$, for ω = 12,000 rpm.

3.4 Flow Structure & Quality

The $\vec{u}$ vector field for the entire fluid volume for the ω = 12,000 rpm case is shown in Fig. 9. For this case, fluid flows through the inlets at ~0.5 m/s. The rotation of the rotor causes the fluid in the annulus between the rotor and the casing to also rotate in the same direction. The absolute velocity of the fluid in this annulus increases from nearly zero at the casing wall to 15 m/s at the rotor wall, about the axis of rotation. Fluid is drawn through the center of the rotor towards the impeller core, where it is pulled into the impeller and accelerated toward the outlets. Fluid reaches a maximum velocity of 12 m/s at the vane tips and is decelerated by the body force imposed by the outlet walls, slowing to 0.5 m/s.

The flow at the impeller for ω = 800 rpm with a rotating reference frame and ω = 12,000 rpm with a rotating reference frame as well as with a rotating mesh is shown in Fig. 10. As expected, the absolute velocity of the fluid increases with increasing pump speed, as does static pressure at the outlets. The $\vec{u}$ vector plots show fluid entering the domain between vanes and turning into the direction of the impeller's rotation, with velocity magnitude increasing with

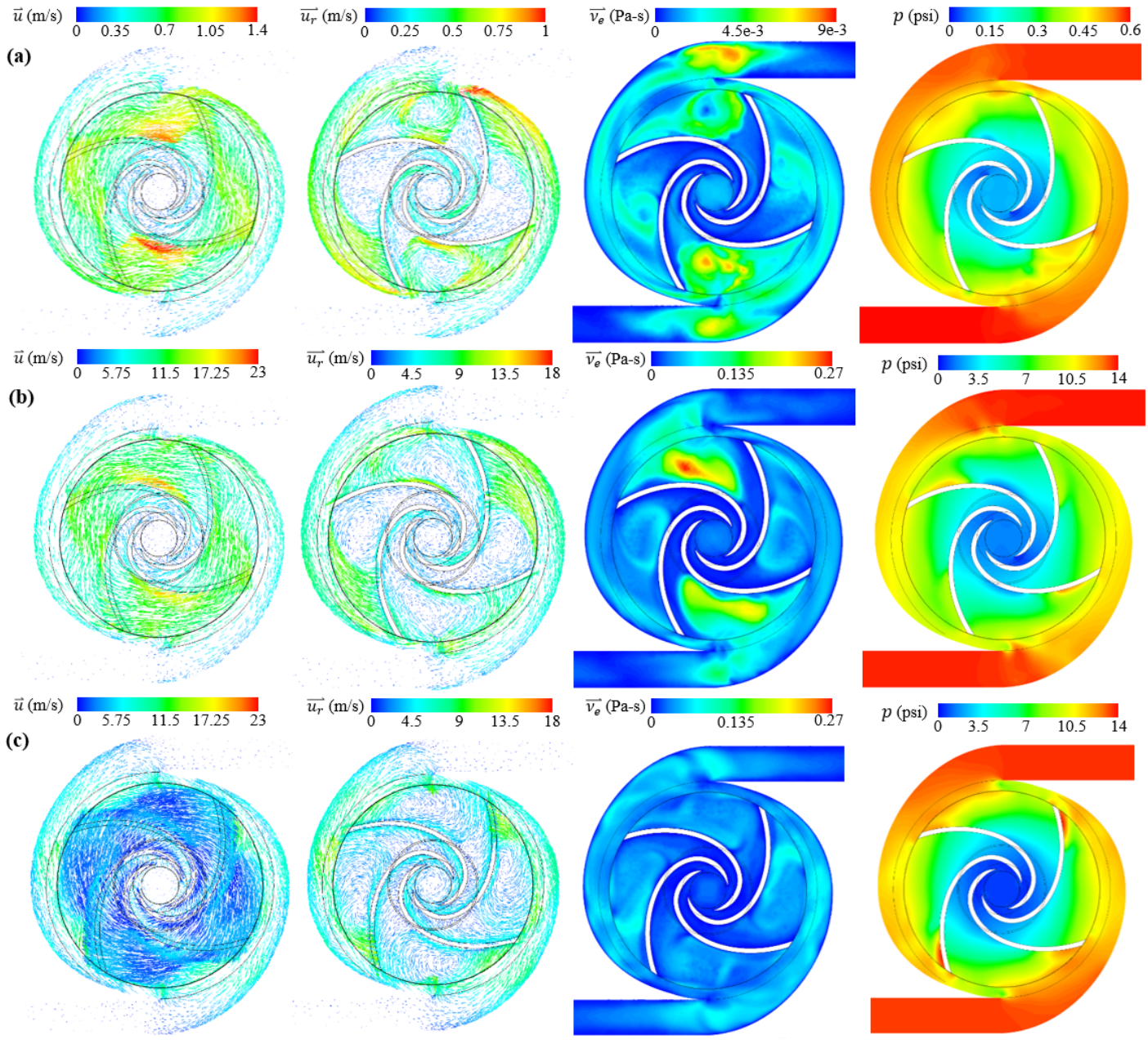

Fig. 10. Vector plots of $\vec{u}$ and $\vec{u_r}$ and contour plots of ν_e and p for (a) ω = 800 rpm (b) ω = 12,000 rpm with rotating reference frame (c) ω = 12,000 rpm with rotating mesh.

radial distance from the impeller core. Peak $\vec{u}$ is seen at the vane tips and towards the center of the vane walls at the vanes immediately upstream of the impeller outlets. Although the $\vec{u}$ field is aligned in the direction of rotation in all cases, the $\vec{u_r}$ field shows the relative velocity opposing the bulk flow, with the formation of vortices in the fluid between vanes. The strength of the vortices, as measured by ν_e, increases with pump speed. The highest ν_e is seen in the outlets and in the domain between the vanes directly upstream of the outlets. Static pressure follows the expected trend, with Δp from the impeller core to the outlets increasing with pump

speed. A sharp decrease in velocity from the vane tips to the outlet stems results in a 30% increase in static pressure for all cases. A Δp of 14.18 psid is predicted for the pump's design point with ammonia at 12,000 rpm.

The vector plots of $\vec{u}$ in the case of ω = 12,000 rpm show agreement in the general flow structure between rotating reference frame (Fig. 10(b)) and rotating mesh (Fig. 10(c)) methods. Absolute velocity is slightly lower in the domain between vanes for the rotating mesh case. The $\vec{u_r}$ plots show the formation of vortices in the same locations, however they extend further toward the vane tips in the case with a rotating mesh. Eddy viscosity is more uniform throughout the impeller and outlet stems with a rotating mesh, with a maximum ν_e of $\sim$ 0.1 Pa-s. Localized peaks in ν_e of 0.2 - 0.25 Pa-s are observed in the vortex centers in the case with a rotating reference frame, indicating that this method of simulating rotation results in formation of stronger vortices than using a rotating mesh. Contour plots of static pressure agree well, with localized peaks at the vane tips being more noticeable in the case with a rotating mesh. Despite these subtle differences in flow structure, the overall flow is qualitatively similar between the two methods.

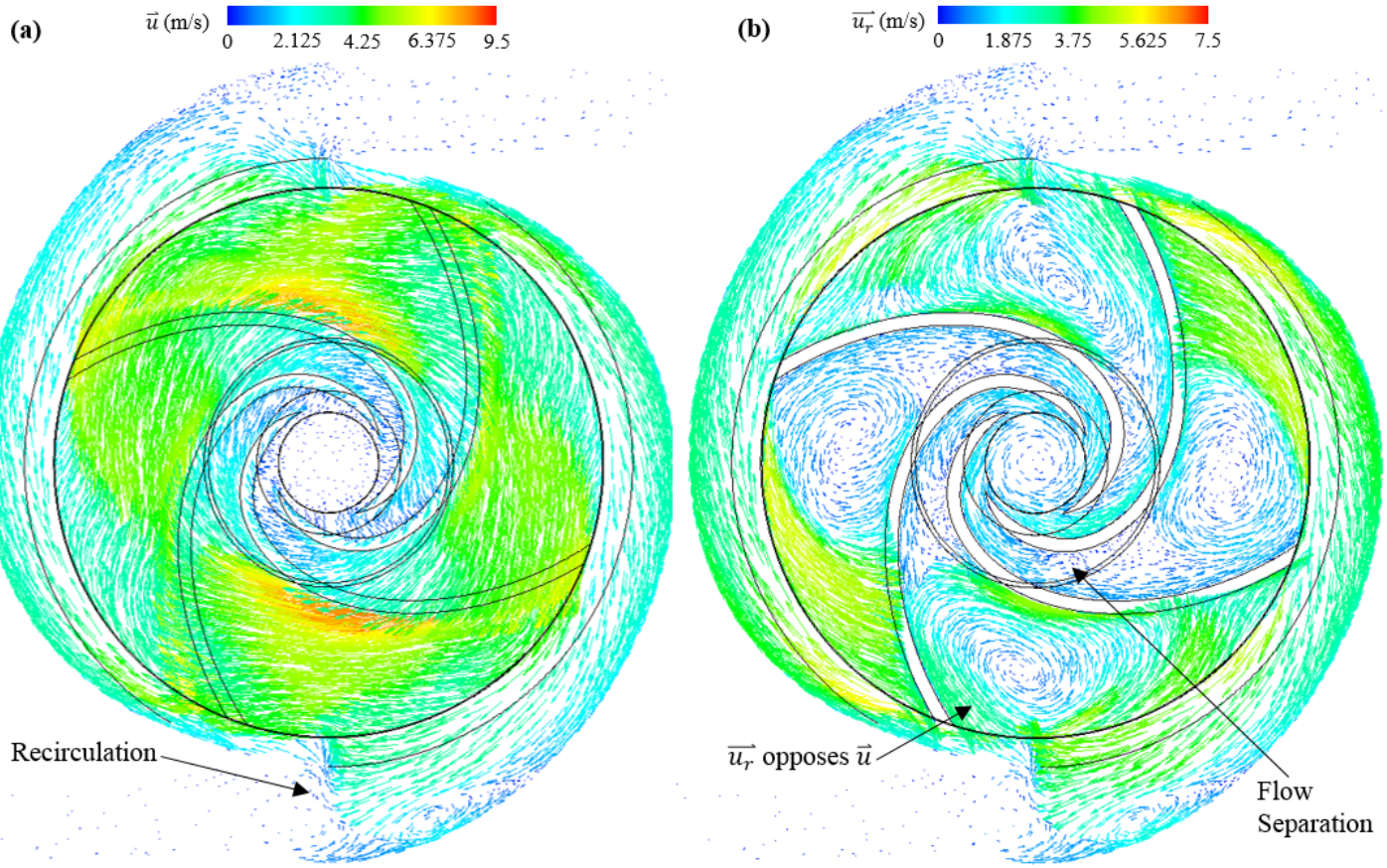

Fig. 11. Vector plots of (a) $\vec{u}$ and (b) $\vec{u_r}$ for ω = 5,600 rpm with Freon as the working fluid.

Figure 11 shows vector plots of $\vec{u}$ and $\vec{u_r}$ for the case with Freon at ω = 5,600 rpm. The flow structure is the same as that seen with ammonia. The bulk velocity is in the direction of rotation and directed into the outlet stems, however, recirculation is evident as fluid traveling into the outlet stem is pulled back into the impeller, as marked in Fig. 11(a). This recirculation was also seen in all ammonia cases. In order to gauge the quality of flow through the impeller, $\vec{u_r}$ may be a better indicator of design flaws. Figure 11(b) shows the formation of vortices in the impeller, relative to the direction of rotation. Flow separation from the vane walls occurs at the location of steepest curvature, likely contributing to the formation of vortices and recirculation as visible in the rotating reference frame.

3.5 Vane Design Study

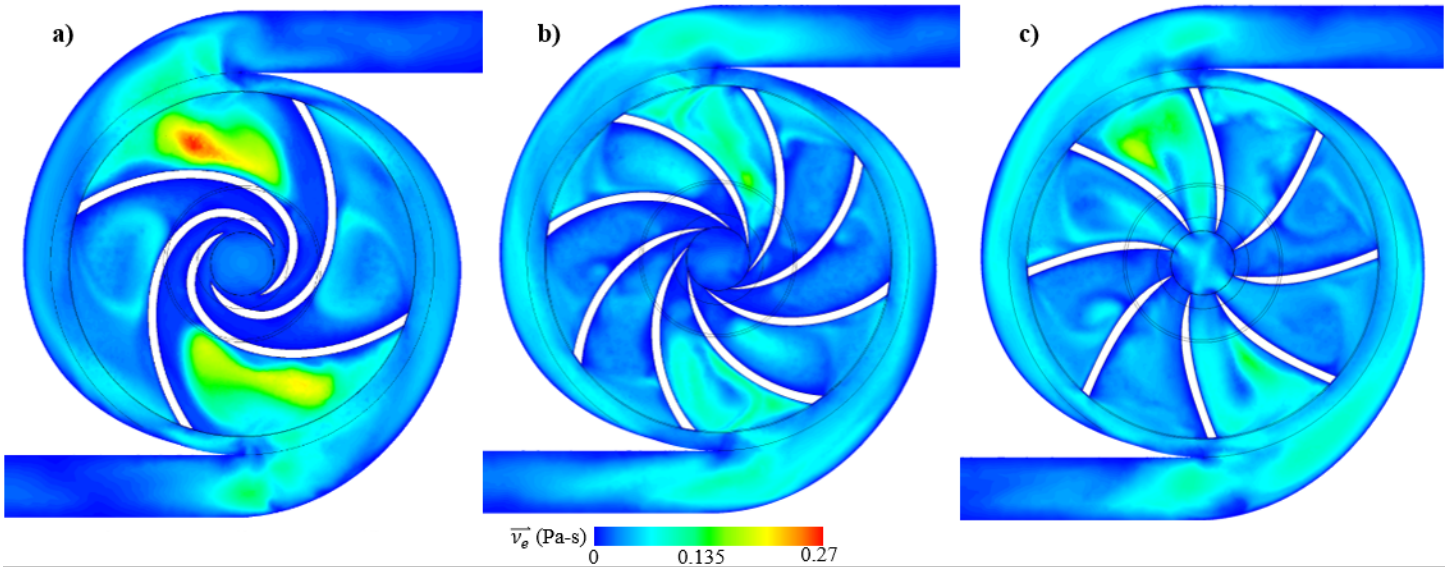

Fig. 12. Eddy viscosity contours for ω = 12,000 rpm with rotating reference frame for the (a) original impeller and (b & c) potential redesigns.

Figure 12 shows contour plots of ν_e for ω = 12,000 rpm with the original impeller design and two potential redesigns. Both redesigned impellers have eight vanes instead of four, with reduced curvature in impeller (b) and minimal curvature in impeller (c). The intent of doubling the number of vanes and reducing the curvature was to investigate the possibility that the steep curvature in the original impeller design caused flow separation along the vane walls that resulted in the formation of vortices. The contour plots show that the magnitude of ν_e peaks near the pump outlets for all three designs, but the peak ν_e is reduced with a greater number of vanes, from 0.27 Pa-s in the original design to 0.15 in redesign (b) and 0.17 in redesign (c).

Table 3. Results for ω = 12,000 rpm with all impeller designs.

Impeller	Peak ν_e (Pa-s)	Avg. ν_e (Pa-s)	T (oz-in)	η	Δp (psi)
Original (a)	0.27	0.0344	3.69	0.036	14.2
Redesign (b)	0.15	0.0304	3.42	0.038	13.9
Redesign (c)	0.17	0.0331	3.46	0.037	13.8

Despite the reduction in peak ν_e, there is little change to ν_e when taken as the area-weighted average across a plane that cuts through the impeller center (the plane shown in Fig. 12). The peak and average values for ν_e, T, η, and Δp are shown in Table 3. Although the redesigns do result in less recirculation in the impeller, the changes to the impeller design did not have a significant effect on pump efficiency or torque requirement.

3.6 Closed Loop System

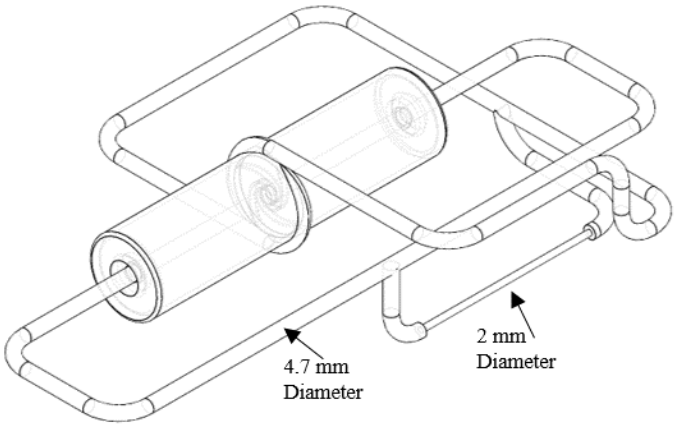

Fig. 13. Closed loop system with constricted section.

In order to evaluate the effect of the mass inflow boundary conditions on the pump performance, additional simulations were run for ω = 2,800 rpm with a closed loop system, as shown in Fig. 13. No inflow or outflow boundary conditions were required, due to the direct connection of the pump outlets to the inlets. Rotation of the impeller was initialized as previously described with a rotating reference frame. Two simulations were run with this configuration. In the first, the pipe diameter was not constricted anywhere along the flowpath and maintained at a constant 4.7 mm. In the second, a 68 mm length of pipe was constricted to a diameter of 2 mm, as shown in Fig. 13. The constriction was added to increase the pressure drop across the loop, to verify that the pressure head across the impeller would show a corresponding increase.

In the simulation with a constant diameter loop, the pump produced a Δp = 0.33 psi with

a $\dot{m} = 15$ g/s. This value of Δp is only 55% of the predicted value of 0.596 psi, so the loop was modified with the constricted section to decrease $\dot{m}$. If operating as designed, the reduction in mass flowrate was expected to result in a corresponding increase in Δp across the pump. The simulation results with the constricted section did indeed show an increased Δp of 0.72 psi and a decreased $\dot{m}$ of 6 g/s. The closed loop system simulations demonstrated that the pump's performance is independent of the mass inlet inflow and outflow boundary conditions.

4 Alternate Pump Testing

In parallel to the CFD study of the NRL bearingless pump, other options for long-life, maintenance free mechanical pumps were explored. The most promising candidate was a commercially available magnetically coupled bearingless pump. NRL acquired several units and tested their performance with water, R-11, R-134A, ispropyl alcohol, and ammonia.

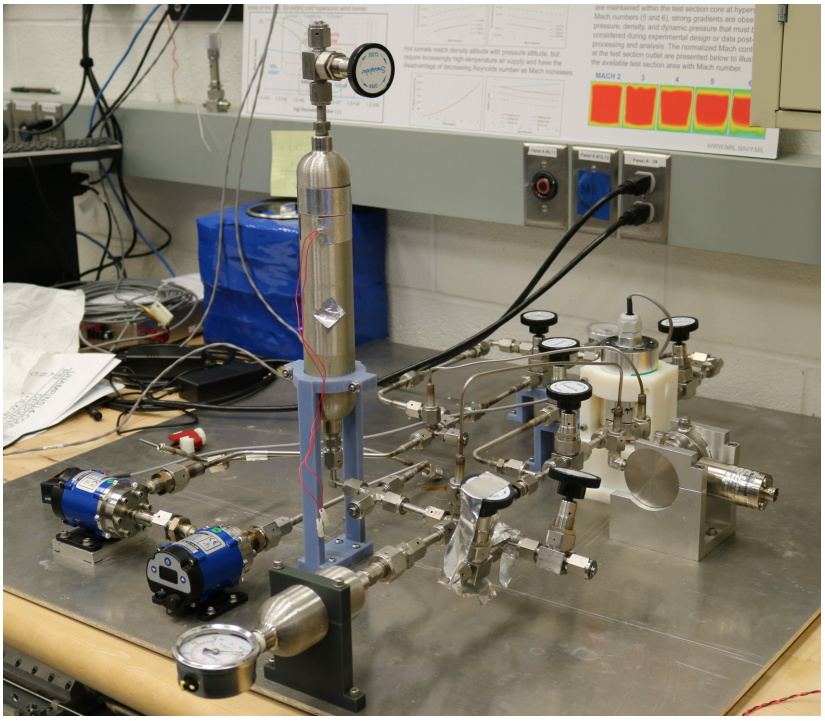

Fig. 14. Loop used for pump testing. Two bearingless pumps are installed in series in the configuration shown.

The loop used for testing the pumps is shown in Fig. 14 and the results are shown in Figs. 15-17. The test loop was equipped with an expansion tank, absolute pressure gauge, differential pressure gauge across the pump(s), and flowmeter. A gate valve was used for increasing or decreasing pressure loss in the liquid transport lines, but in all data contained in this report all valves were fully open.

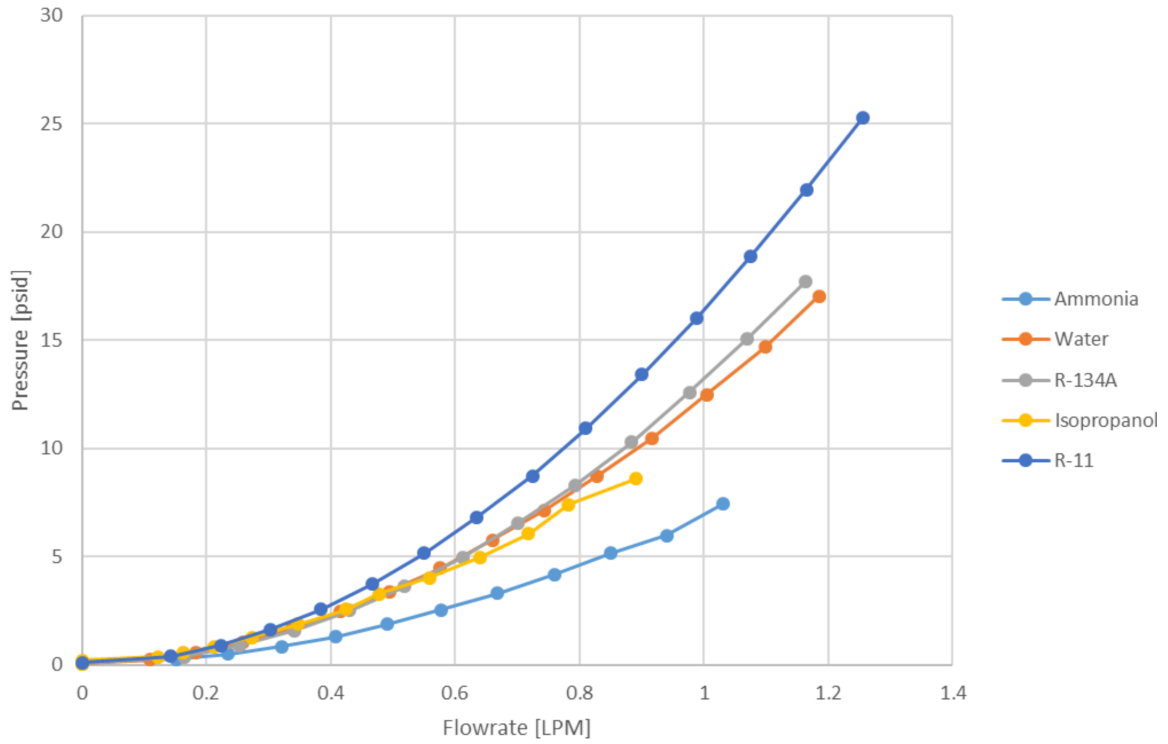

Fig. 15. Pressure head vs. flowrate curves for the bearingless pump with several working fluids.

Figure 15 shows the pressure head vs. flowrate for the bearingless pump with all working fluids tested. In each test, the pump motor was ramped to its maximum speed of 15,000 RPM in 1,000 RPM increments. The pressure and flowrate generated by each fluid scale with fluid density, with the densest fluid, R11, producing the greatest pressure head and flowrate for a given pump speed. The performance is comparable among all fluids. Although the pump generated the lowest pressure head and flowrate with ammonia, the performance is still expected to be sufficient for a hybrid loop heat pipe application.

Two of the bearingless pumps were installed in series to assess the performance gains when both pumps were running as well as the pressure loss through an inoperable pump when only one of the two pumps were running. Testing in this configuration was important for assessing the suitability of the pump for installation on a flight system, as several pumps would likely need to be installed in series for redundancy and reliability. Figure 16 shows pressure head versus flowrate with R-134A working fluid. The curve in orange shows the pressure head and flowrate through two pumps in series with only one pump operating. The blue data points correspond to the performance of a single operating pump, not in series with another inoperable pump. The purpose of this test was to asses the reduction in pressure head and flowrate caused by flowing through an inoperable pump. From Fig. 16 it is evident that there is a very slight loss

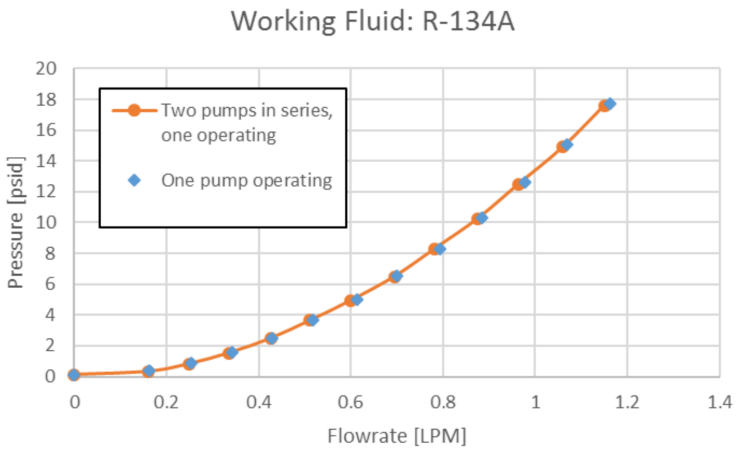

Fig. 16. Pressure head vs. flowrate for a single pump with R-134A as the working fluid. Two configurations shown: (orange) two pumps in series, one operating (blue) single pump operating, not in series with another pump.

in pressure head generated when flowing through an inoperable pump, but this performance decrease is slight enough to be considered negligible. This result indicates that many pumps can be installed in series for redundancy without a significant decrease in pressure head available in the system if one or more pumps are inoperable.

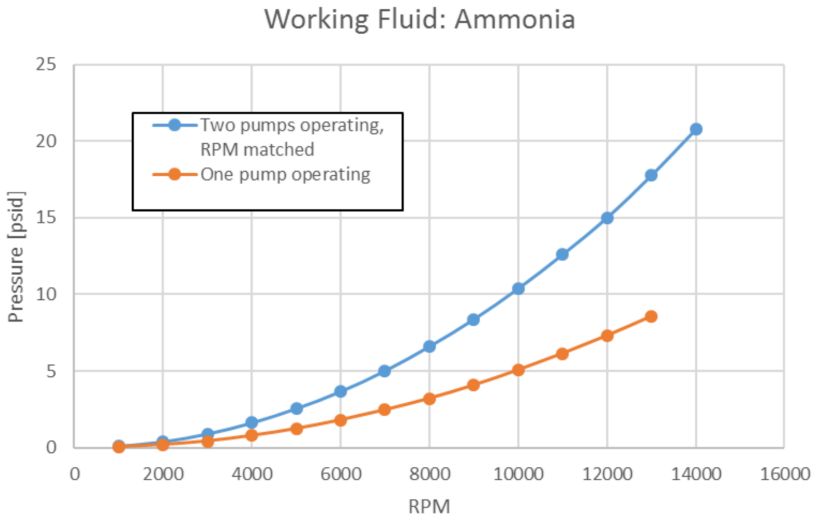

Fig. 17. Pressure head vs. flowrate for two pumps in series with ammonia as the working fluid.

In addition to using multiple pumps in series for redundancy, they can generate greater pressure head than a single pump alone. In a hybrid loop heat pipe system, this would allow for greater heat transport capacity. Because the lowest pressure head for a given pump speed was observed with ammonia, the lowest density fluid tested, it was selected as the working fluid for testing two pumps operating in series. The results are shown in Fig. 17, where the blue curve shows the performance with both pumps operating at the same speed. The orange

curve shows the performance with only a single pump operating (not in series with another) for comparison. At a given pump speed, the pressure head generated by two pumps in series is roughly double what is generated by a single pump alone. It is likely that, for an ammonia hybrid loop heat pipe system, two pumps operating in series would provide sufficient pressure head for the highest heat loads encountered.

5 Discussion

The computational model reproduced the experimental results with Freon, generating a pressure head of 6.26 psi at an operating speed of 5,600 rpm. Simulation results also agree with the theoretical performance predictions for pressure head as a function of pump speed, or ω. The simulations showed significant recirculation in the impeller, likely a result of flow separation from the vanes due to a steep curvature of the vane walls. The strength of the vortices generated in the impeller increased with ω. Pump efficiency was low, reaching an asymptotic value of $\sim$3.5% and torque required to spin the rotor at the designated speed increased at a rate of ω^2. Optimization of the impeller design, including number of vanes and vane wall curvature, is required to reduce recirculation in the impeller and improve pump efficiency. The electromagnetic motor was designed to generate 1.9 oz-in of torque at a speed of 11,500 rpm. This design limitation was exceeded in the simulations, where 3.5 oz-in was required to spin the rotor at 11,500 rpm. With the current impeller design, the recirculation and turbulence within the impeller is significant and the pump efficiency is low. It is likely that the high torque requirements are related to the recirculation in the impeller and that these phenomena contribute to the failure of the pump with ammonia.

The CFD results indicate that the pump should produce a significant pressure head with ammonia, however, the CFD model is constrained to maintain a constant impeller position. As such, in the simulations the rotor is always centered within the pump casing and the inertial response of the free-floating rotor to the surrounding flow is not accurately captured. This is an unfortunate limitation of current CFD capabilities, however, it points to the importance of centering the rotor in the casing in generating a pressure head with the NRL bearingless pump. Therefore, the most likely cause of failure with ammonia is the failure of the flow to center the impeller in the casing. If the rotor is centered within the casing during operation with Freon and not with ammonia, it is likely that the failure is buoyancy-related. Freon has over twice

the density of ammonia and therefore produces twice the buoyancy force on the rotor for a given volume of fluid displacement. A greater buoyancy force on the rotor would result in more stable operation of the pump even if the rotor is not dynamically balanced and has a tendency to move off-center during operation.

A redesign of the NRL bearingless pump is likely required in order to successfully run the pump with ammonia. The redesign should focus on reducing the aspect ratio (length/outside diameter) of the rotor while still maintaining a large rotor volume for buoyancy in a low-density fluid. The current rotor design has an aspect ratio of 4.5. Any mass imbalances at the ends of the rotor would contribute significantly to the development of dynamic instabilities due to the large moments they would impose on the rotor. Reducing the aspect ratio would serve to reduce this effect. However, given that an alternative to the NRL bearingless pump was successfully tested (see Sec. 4)with a variety of working fluids, including ammonia, a redesign of the pump is not an immediate priority.

6 Future Work: Hybrid Loop Testing

A bench test hybrid loop heat pipe was designed with the intent of testing the increase in heat transport capacity achieved through integration of a mechanical pump. The drawing for the loop is shown in Fig. 18. In addition to the evaporator, which generates pressure head in the system through capillary action as in a traditional loop heat pipe [7], two of the commercially available bearingless pumps are installed in series to provide pressure head similar to that obtained during the performance characterization tests with results shown in Figs. 15-17.

The evaporator has one inlet (liquid phase) and two outlets (liquid and vapor phases). The addition of a liquid outlet, not typically used in loop heat pipe evaporators, allows for the free flow of working fluid through the evaporator. This is necessary in the event that the mechanical pumps are generating a flowrate in excess of the rate at which the fluid evaporates, which is dependent on both the pump speeds and the heat load applied to the evaporator. Both the evaporator and heat exchanger are sized to accommodate heat loads of up to 5 kW. The wick in the evaporator was made of 1.2 μm sintered nickel (35%) porosity, with a 0.5 in. outside diameter and length of 18 in.

At the time this report was written, the loop components were being purchased or machined. Once fabrication is completed, testing will begin in the Advanced Two-Phase Facility at the

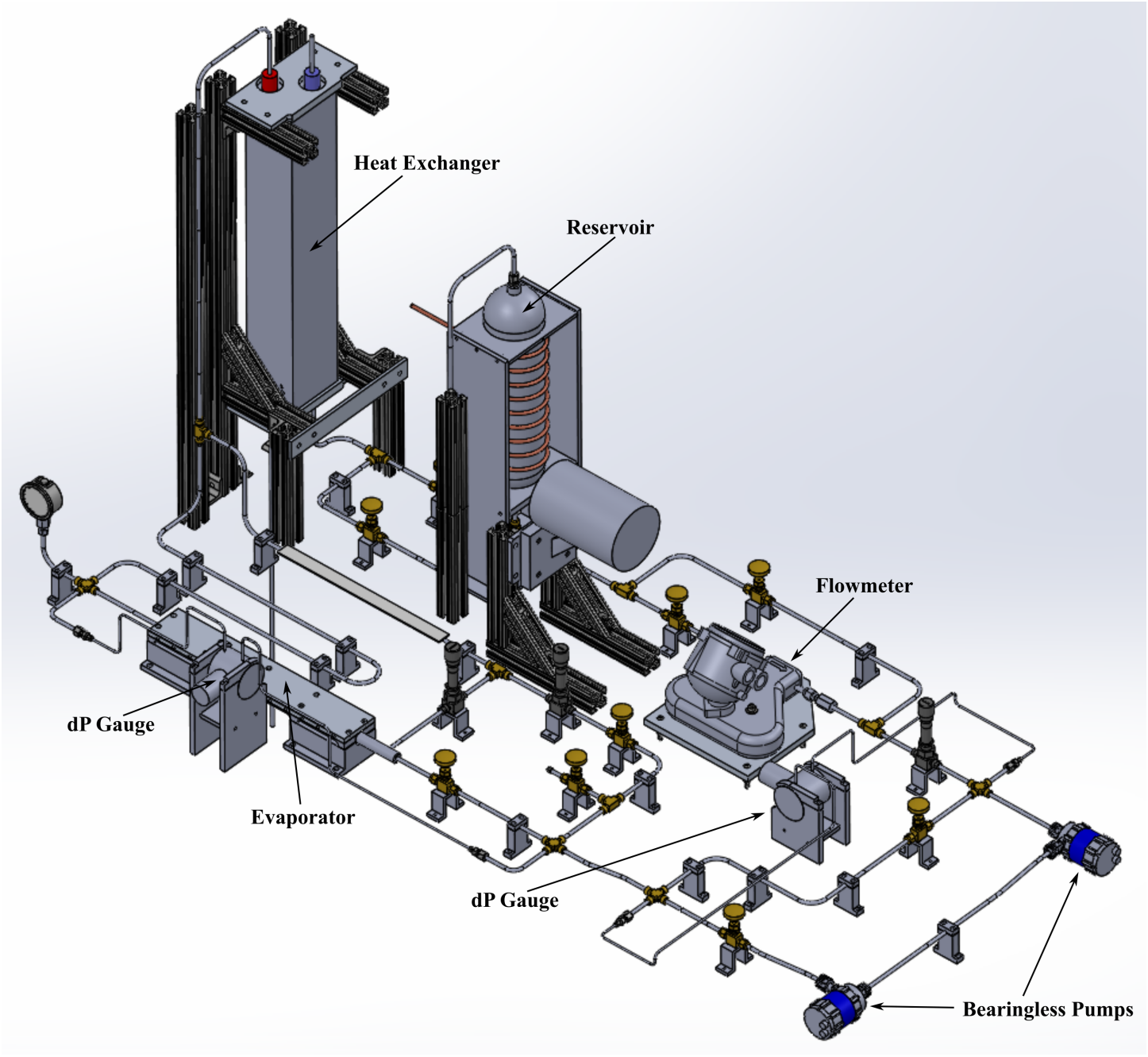

Fig. 18. Pressure head vs. flowrate for two pumps in series with ammonia as the working fluid.

Naval Research Laboratory. The overall test goal is to determine the maximum heat transport capacity of the loop without the assistance of mechanical pumping, then characterize the increase in heat transport capacity that is achievable through the addition of mechanical pumps. Several working fluids will be tested, but the primary fluid to be used in the majority of testing will be ammonia due to its superior latent heat of vaporization and liquid transport factor, as discussed in Sec. 1.

7 Summary & Conclusions

In order to increase the heat transport capacity of loop heat pipes for thermal management of high-heat-flux systems, there has been significant interest in the integration of a mechanical pump into a traditional capillary-pumped loop heat pipe. The primary requirement for the mechanical pump, aside from generating adequate pressure and flowrate, is to be maintenance-free and long-life so as to not compromise the service life of a thermal management system aboard an unmanned spacecraft. Two candidate pump designs were explored in this paper: the NRL bearingless pump and a commercially available magnetically-coupled bearingless pump.

A model was developed to simulate the flow through NRL pump. The pump was designed to require no bearing, seal, or lubrication and therefore be maintenance-free and long-life. The pump is low-flowrate and intended to produce a relatively small pressure head to supplement a capillary-pumped loop heat pipe system. During initial bench-tests, the pump succeeded in meeting performance estimates with a Freon equivalent as the working fluid, but failed to produce a pressure head with ammonia as a working fluid. Computational fluid dynamics simulations were performed to investigate the cause of failure with ammonia.

The model reproduced the experimental results with Freon, matching pressure and flowrate data despite the presence of significant turbulence in the impeller. Simulation results also agree with the theoretical performance predictions for pressure head as a function of pump speed. Simulations with ammonia as the working fluid did not give an indication of failure. However, the inertial response of the buoyant rotor to the fluid was not modeled in the simulations, due to a lack of modeling capability. As such, in all simulations the rotor stays perfectly centered in the casing. This is the main difference between the simulations and experiments and thus the most likely cause of failure of the pump to generate pressure head: the rotor does not stay centered and coupled with the electromagnetic motor. Based on this investigation, it is suspected that the lower bouyancy force acting on the pump with ammonia than with Freon (due to differing fluid densities) resulted in the rotor becoming dynamically unbalanced with ammonia as the working fluid.

An alternative magnetically driven bearingless pump design, available commercially, was considered for integration into a loop heat pipe and tested in the NRL Advanced Two Phase Facility. The pump was found to operate successfully with a variety of working fluids, including ammonia, producing substantial flowrate and pressure head in a small frame with a lower power

requirement. Two pumps were tested in series, generating roughly double the pressure head of a single pump. Additionally, the pressure loss for flow through an inoperable pump is negligible, allowing many of the units to be installed in series for increased performance or redundancy. Based on these results, this pump was selected for integration into a hybrid mechanically pumped loop heat pipe.

Acknowledgments

This work was made possible through the Karle's Fellowship Program at the US Naval Research Laboratory.

References

[1] Izraelev, V., "Bearing and Seal-Free Blood Pump. US Patent No. 5,685,700," Filed Jun. 1, 1995.

[2] Izraelev, V., "Pump assembly with bearing and seal-free reusable impeller for fragile and agressive fluids. US Patent No. 6,547,539," Filed May 21, 2007.

[3] Izraelev, V., "Seal and bear-free fluid pump incorporating a passively suspended self-positioning impeller. US Patent No. 7,052,253," Filed May 19, 2003.

[4] Shepherd, D., *Principles of Turbomachinery*, Macmillan Publishing Co., Inc., New York, NY, 1956.

[5] Kundu, P. and Cohen, I., *Fluid Mechanics*, Elsevier Academic Press, San Diego, CA, 2004.

[6] Munson, B., Young, D., and Okiishi, T., *Fundamentals of Fluid Mechanics*, John Wiley & Sons, Inc., Hoboken, NJ, 2010.

[7] Hoang, T. T., Baldauff, R. W., and Cheung, K. H., "Hybrid Two-Phase Mechanical/Capillary Pumped Loop for High-Capacity Heat Transport," Tech. rep., SAE Technical Paper, 2007.